A Journal of the Gesellschaft Deutscher Chemiker

Angewandte International Edition Chemie

GDCh

www.angewandte.org

Accepted Article

Title: pH-amplified CRET nanoparticles for in vivo imaging of tumor metastatic lymph nodes

Authors: Zenghui Wang, Heming Xia, Binlong Chen, Yaoqi Wang, Qingqing yin, Yue Yan, Ye Yang, Mingmei Tang, Jianxiong Liu, Ruiyang Zhao, Wenzhe Li, Qiang Zhang, and Yiguang Wang

To be cited as: *Angew. Chem. Int. Ed.* 10.1002/anie.202102044

Link to VoR: https://doi.org/10.1002/anie.202102044

WILEY-VCH

10.1002/anie.202102044

WILEY-VCH

RESEARCH ARTICLE

pH-amplified CRET nanoparticles for *in vivo* imaging of tumor metastatic lymph nodes

Zenghui Wang, [a, b] Heming Xia, [a, b] Binlong Chen, [a, b] Yaoqi Wang, [b] Qingqing Yin, [b] Yue Yan, [b] Ye Yang, [b] Mingmei Tang, [b] Jianxiong Liu, [b] Ruiyang Zhao, [b] Wenzhe Li, [a] Qiang Zhang [a, b] and Yiguang Wang [a, b]*

[a] Z. Wang, H. Xia, Dr. B. Chen, Dr. W Li, Prof. Q. Zhang, Prof. Y. Wang
State Key Laboratory of Natural and Biomimetic Drugs, School of Pharmaceutical Sciences, Peking University
Beijing 100191, China
E-mail: yiguang.wang@pku.edu.cn

[b] Z. Wang, H. Xia, Dr. B. Chen, Y. Wang, Q. Yin, Y. Yan, Y. Yang, M, Tang, J. Liu, R. Zhao, Prof. Q. Zhang, Prof. Y. Wang
Beijing Key Laboratory of Molecular Pharmaceutics, School of Pharmaceutical Sciences, Peking University
Beijing 100191, China

Supporting information for this article is given via a link at the end of the document.

Abstract: Noninvasive imaging strategies have been extensively investigated for *in vivo* mapping of sentinel lymph nodes (SLNs). However, the current imaging strategies fail to accurately assess tumor metastatic status in SLNs with high sensitivity. Here we report pH-amplified self-illuminating near-infrared nanoparticles, which integrate chemiluminescence resonance energy transfer (CRET) and signal amplification strategy, enabling accurate identification of metastatic SLNs. After draining into lymph nodes, the nanoparticles were phagocytosed and dissociated in acidic phagosomes of inflammatory macrophages to emit near-infrared luminescent light. Using these nanoparticles, we successfully differentiated tumor metastatic lymph nodes from benign ones. These nanoparticles also exhibited excellent imaging capability for early detection of metastatic SLNs in diverse animal tumor models with small tumor volume (100-200 mm^3).

Introduction

For cancer patients, the sentinel lymph nodes (SLNs) are often the first station of tumor metastasis. Accurate identification of metastatic SLNs at an early stage, before systematic metastasis, is of great significance for symptomatic treatment and prognosis.[1] Clinically, intraoperative lymphangiography and sentinel lymph node biopsy are often used as the gold standards for lymphatic metastasis detection.[2] However, the use of radioactive isotopes, such as technetium-99m, will inevitably bring up some concerns to cancer patients, although the radiation dose is relatively low.[3] In addition, intraoperative SLN biopsy is a time-consuming procedure.[4] Recently, several antibody-fluorophore conjugated probes targeting cancer cell specific biomarkers have been reported for the visualization of metastatic SLNs during surgery.[5] However, owing to the high heterogeneity of tumor-specific biomarkers within and between different cancer types,[6] antibody-mediated imaging agents can not accurately identify metastatic lymph nodes in all tumor types. Therefore, there is an urgent need to develop a noninvasive imaging strategy with high sensitivity for identification of tumor lymphatic metastasis.[7]

It has been demonstrated that the phagocytes reside in SLNs are activated regardless of tumor type during tumor lymphatic metastasis.[8] Thus, accurate detection of over-activation signals of phagocytes may be a potential strategy for the universal and early diagnosis of tumor metastasis.[9] Myeloperoxidase (MPO) activity is highly upregulated in inflammatory diseases, such as cancer and atherosclerosis.[10] Several luminol-mediated bioluminescence imaging (BLI) of MPO activity have been reported for the visualization of inflammatory diseases.[11] In the BLI imaging modality, luminol acts as an MPO-specific probe, emitting a dazzling blue light ($\lambda_{max} \approx 425$ nm) when exposed to the MPO, a biomarker of activated phagocytes.[12] To further enhance the penetration depth of blue luminescence signals, nanoparticle-based chemiluminescence resonance energy transfer (CRET) or bioluminescence resonance energy transfer (BRET) imaging methodologies have been proposed.[13] However, most nano-systems are designed to be non-responsive, which may cause signal attenuation due to aggregation-caused quenching (ACQ).[14]

Herein, we introduced a Super-**p**H-Responsive **C**RET **N**anosensors (PCN) for noninvasive identification of tumor metastatic status in sentinel lymph nodes by integrating CRET and pH-responsive signal amplification strategy (Scheme 1). In this strategy, luminol and a near-infrared (NIR) fluorescent probe pyropheophorbide a (PPa),[15] were covalently conjugated to pH-responsive nanoparticles, which have been demonstrated to possess excellent pH responsiveness[16] and subcellular targeting capability[17] in our previous works. In the current work, we hypothesized that the luminol component would precisely report the activity of MPO of macrophage in metastatic SLNs and emit blue luminescence (Scheme S2); the PPa component can relay the blue luminescence to emit NIR light through CRET ($\lambda_{max} \approx 730$ nm);[18] PCN can respond to phagosomal acidity to amplify the luminescence signals for visualization of metastatic SLNs. A series of PCNs with different transition pH (pH_t) were developed to target distinct phagosome maturation stages upon phagocytosis by macrophage. Under neutral and alkaline conditions, PCNs exhibit as stable nanoparticles through hydrophobic interactions and keep silent owing to ACQ effect of acceptor molecule (OFF state).[19] Once PCN is drained to the

10.1002/anie.202102044

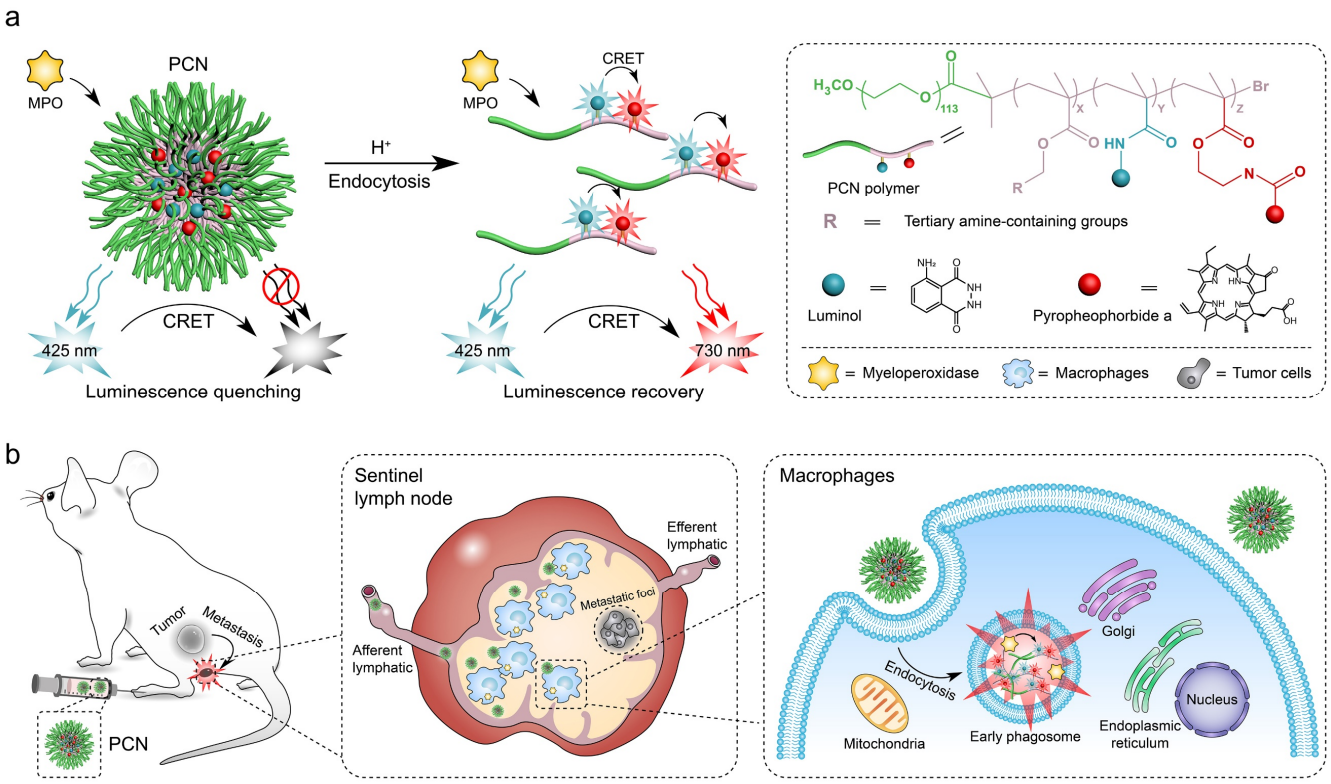

Scheme 1. The schematic design and work mechanism of pH-amplified self-illuminating PCN for the detection of tumor metastasis in sentinel lymph nodes in living mice. a) The luminescence signal of PCN is quenched at pH 7.4 due to ACQ effect. As the pH decreases, the nanoparticle is disassembled at pH < pH_t, and the NIR luminescence signal is recovered through efficient intramolecular CRET. b) Tumor metastasis in sentinel lymph nodes can be detected by pH-amplified luminescence imaging with high sensitivity and specificity. Tumor metastasis causes inflammation of the sentinel lymph node. After injection in the hind paws, PCN can effectively drain to the inflamed SLN. Once phagocytosis by activated macrophages, PCN can be disassembled in acidic phagosome and then catalyzed by overexpressed MPO to emit strong luminescence. CRET = chemiluminescence resonance energy transfer, MPO = myeloperoxidase, ACQ = Aggregation caused quenching.

SLNs and taken up by activated macrophages, the acidity at different phagosome maturation stages will immediately trigger the disassembly of nanoparticles. Subsequently, luminol is oxidized by MPO-catalyzed hypochlorous acid in phagosome, thereby emitting NIR light via CRET (ON state) for self-luminescence imaging of tumor metastasis in lymph nodes with greatly improved specificity and sensitivity.[20] We reported a pH-responsive CRET nanoparticle imaging strategy for the first time and found that phagosome-targeted self-illuminating nanoparticles could significantly amplify the luminescence signals for visualization of metastatic lymph nodes.

Results and Discussion

Preparation and characterization of PCNs with distinct pK_a

We initially synthesized a series of luminol-encoded amphiphilic block copolymers mPEG-*b*-(PR-*r*-Lum) (abbreviated as PR-Lum), including PC7A-Lum, PEPA-Lum, PDPA-Lum, and PDBA-Lum via atom transfer radical polymerization (ATRP) method[21]. A pH-nonresponsive PEH-Lum polymer was also synthesized as a control (Scheme S1, Figure S1-S7, Table S1).[22] Then, pK_a of these polymers was measured by titration method (Figure 1a).[23] Based on the titration curves, pK_a values for PC7A-Lum, PEPA-Lum, PDPA-Lum, and PDBA-Lum were determined to be 6.86, 6.75, 6.33, and 5.26, respectively. Next, PPa as a CRET acceptor was conjugated to each PR-Lum polymer for the preparation of **PCNs**. Each PCN with a distinct pK_a value was denoted as $PCN_{6.9}$, $PCN_{6.8}$, $PCN_{6.3}$, and $PCN_{5.3}$, respectively. pH-nonresponsive CRET nanosensor was abbreviated as **NPCN**, which composed of PEH-Lum-PPa polymer.

We then chose $PCN_{6.9}$ as a representative to evaluate the pH responsiveness and self-luminescence properties of PCN. Under sonication, PC7A-Lum-PPa polymer self-assembled into a core-shell nanoparticle with a diameter of 35.2 ± 2.6 nm and polydispersity of 0.22 at pH 7.4. At pH 5.4, the $PCN_{6.9}$ was dissociated into unimer with a diameter of about 7 nm (Figure 1b). Transmission electron microscopy (TEM) images also demonstrated that $PCN_{6.9}$ had a spherical structure with a diameter of 33.2 ± 5.9 nm at pH 7.4, and no nanostructure was observed at pH 5.4 (Figure 1c). For NPCNs, the particle size and morphology were pH-independent.

We next explored the MPO-dependent chemiluminescence properties of PCN *in vitro*.[24] Using MPO as a trigger, we collected the luminescence spectra of luminol and PC7A-Lum copolymer.[25] Results showed that both luminol and PC7A-Lum exhibited a maximum emission wavelength at 425 nm (Figure 1d), which proved that the polymerization did not affect the luminescence properties of luminol. Furthermore, there was a considerable spectral overlap between the absorption spectrum of PPa and the luminescence spectrum of PC7A-Lum, enabling efficient

10.1002/anie.202102044

intramolecular CRET from luminol (donor) to PPa (acceptor).[26] The absorption spectrum of $PCN_{6.9}$ exhibited both characteristic peaks for luminol (358 nm) and PPa (413 and 668 nm) (Figure 1e). The luminescence spectrum of $PCN_{6.9}$ was further collected under optimized conditions (Figure 1f).[25] Different from PC7A-Lum, which had single luminescence peak (~ 425 nm), $PCN_{6.9}$ displayed two MPO-triggered luminescence peaks: one peak at ~ 450 nm from the typical luminescence of luminol, and the other peak at ~ 730 nm corresponding to the fluorescence emission of PPa. The luminescence signal of luminol at 450 nm in $PCN_{6.9}$ was significantly reduced as compared with that of PC7A-Lum due to the efficient CRET from luminol to PPa molecules that generated strong NIR luminescence signals. To maximize the luminescence efficiency of $PCN_{6.9}$, the CRET ratio of luminol to PPa in each polymer chain was systemically investigated. A series of PC7A-Lum-PPa polymers with different molar ratios of luminol to PPa were synthesized (Table S1 and S2), and the corresponding self-luminescence curves were shown in Figure 1g. The slight red-shift of the PPa peak may be resulted from the J-aggregate formation in the polymeric micelles with higher PPa contents.[27] The CRET ratios between luminol and PPa were calculated to assess the efficiency of energy transfer.[28] Results showed that the CRET ratio in $PCN_{6.9}$ can reach up to 2.12 (corresponding to an efficiency of 68%), which was very high among that of CRET nanoparticles reported previously.[29]

After demonstrating PCN can induce luminescence in the presence of MPO, we then investigated its luminescence mechanism. The factors affecting luminescence signal were firstly optimized (Figure S8). Then, 4-aminobenzoic hydrazide (4-ABAH) and 2,2,6,6-tetramethylpiperidine-1-oxyl (Tempol) were used to specifically block the functions of MPO and ROS, respectively.[11] With the increasing concentrations of Tempol or 4-ABAH, the luminescence intensity of PCN was gradually reduced (Figure S9), proving that the generation of luminescence were induced by MPO catalyzed oxidation.

To determine whether the luminescence of PCN could exhibit a good pH responsiveness, we captured luminescence images of $PCN_{6.9}$ at different pH values (Figure 1h). At pH higher than 7.0, the luminescence signal of $PCN_{6.9}$ was significantly diminished duo to ACQ effect of PPa molecules at micelle state. Whereas at the pH lower than 6.8, the luminescence signal was dramatically amplified by more than 10-fold, which demonstrated that pH could precisely regulate the luminescence ON/OFF of PCN. In contrast, NPCN nanoparticles exhibited undetectable luminescence signal as a result of pH-independent nanostructure. These results revealed that the micelle dissociation is a prerequisite for the amplification of luminescence signals. To further investigate the

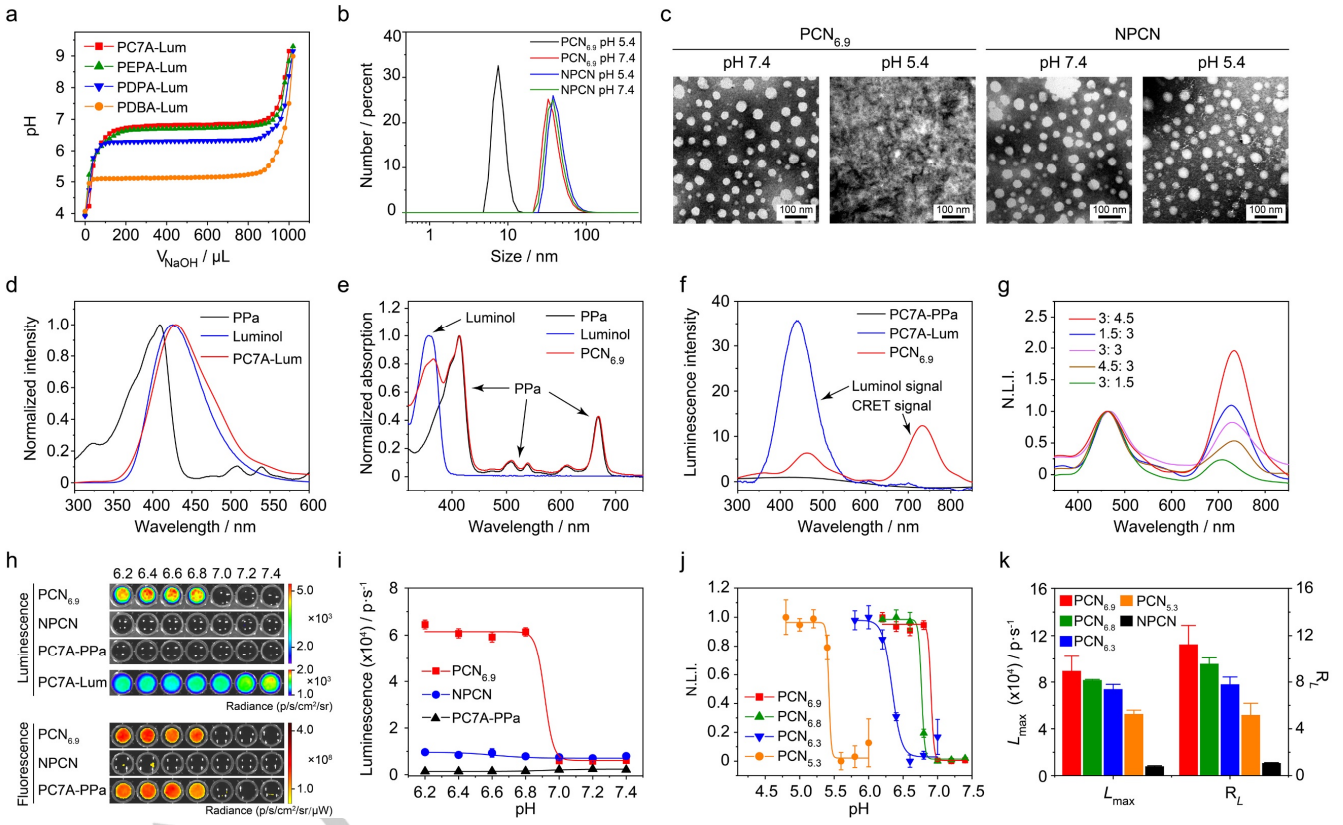

Figure 1. pH-responsiveness and self-luminescence properties of PCNs. a) pH titration curves of PC7A-Lum, PEPA-Lum, PDPA-Lum, and PDBA-Lum polymers. b) Size distribution of $PCN_{6.9}$ and NPCN nanoparticles in pH 5.4 and pH 7.4. c) TEM images of $PCN_{6.9}$ (left) and NPCN (right) in pH 5.4 and pH 7.4. Scale bar = 100 nm. d) The normalized absorption spectrum of PPa in methanol (black) and normalized luminescence spectra of luminol (blue) and PC7A-Lum nanoparticles (red) in PBS. The luminescence spectra were recorded with a spectrophotometer in the presence of 1 U/mL of MPO, 1.25 mM of 4-indophenol, and 50 μM of hydrogen peroxide in PBS. e) The normalized absorption spectra of PPa (black), luminol (blue), and $PCN_{6.9}$ (red) in methanol. f) Luminescence spectra of PC7A-PPa nanoparticle (black), PC7A-Lum nanoparticle (blue), and $PCN_{6.9}$ (red). g) Normalized luminescence spectra of $PCN_{6.9}$ with different ratios of luminol to PPa. Peaks around 425 nm were normalized for comparsion. h) Luminescence images of $PCN_{6.9}$, NPCN, PC7A-PPa and PC7A-Lum nanoparticles in the presence of MPO, 4-indophenol, and hydrogen peroxide and fluorescence images of $PCN_{6.9}$, NPCN and PC7A-PPa nanoparticles. The luminescence sigal of PC7A-Lum is significant lower than that of $PCN_{6.9}$. i) luminescence intensity as a function of pH values for PCN, NPCN, and PC7A-PPa nanoparticles (n = 3). j) Normalized luminescence intensity (N.L.I.) as a function of pH for PCNs. N.L.I. was defined as the value $(L\text{-}L_{min})/(L_{max}\text{-}L_{min})$ (n = 3). k) Maximum luminescence intensity (L_{max}) and ON/OFF ratio (R_L) for each PCN. All data are represented as mean ± s.d.

10.1002/anie.202102044

WILEY-VCH

RESEARCH ARTICLE

underlying mechanism of pH-responsive luminescence emission of PCNs, the fluorescence image of PC7A-PPa and luminescence image of PC7A-Lum were also captured. The results demonstrated that luminescence quenching of PCN at higher pHis due to ACQ effect of PPa rather than the quenching of self-luminescence of luminol. To quantitatively assess the pH responsive properties of PCN, luminescence intensity vs. pH curve was plotted (Figure 1i). In the above curve, the pH transition (pH_t) was defined as the pH value corresponding to 50% of the maximum self-luminescence signal is recovered. The pH_t of PCN was determined to be 6.90 with a very sharp responsiveness (0.2 pH unit). The ratio of L_{max} and L_{min} (R_L = L_{max}/L_{min}) was also measured to evaluate the luminescence recovery between ON and OFF states, where L_{max} and L_{min} were the maximal and minimal luminescence intensities among ON and OFF states. R_L and L_{max} of polymers with different luminol to PPa ratios were listed in Table S2. To achieve high CRET ratio, R_L, and L_{max}, PCNs with a luminol to PPa ratio of 3: 4.5 was selected for further investigation, which presented 11.25-fold signal amplification capability (Figure S10). Furthermore, another NIR fluorescent

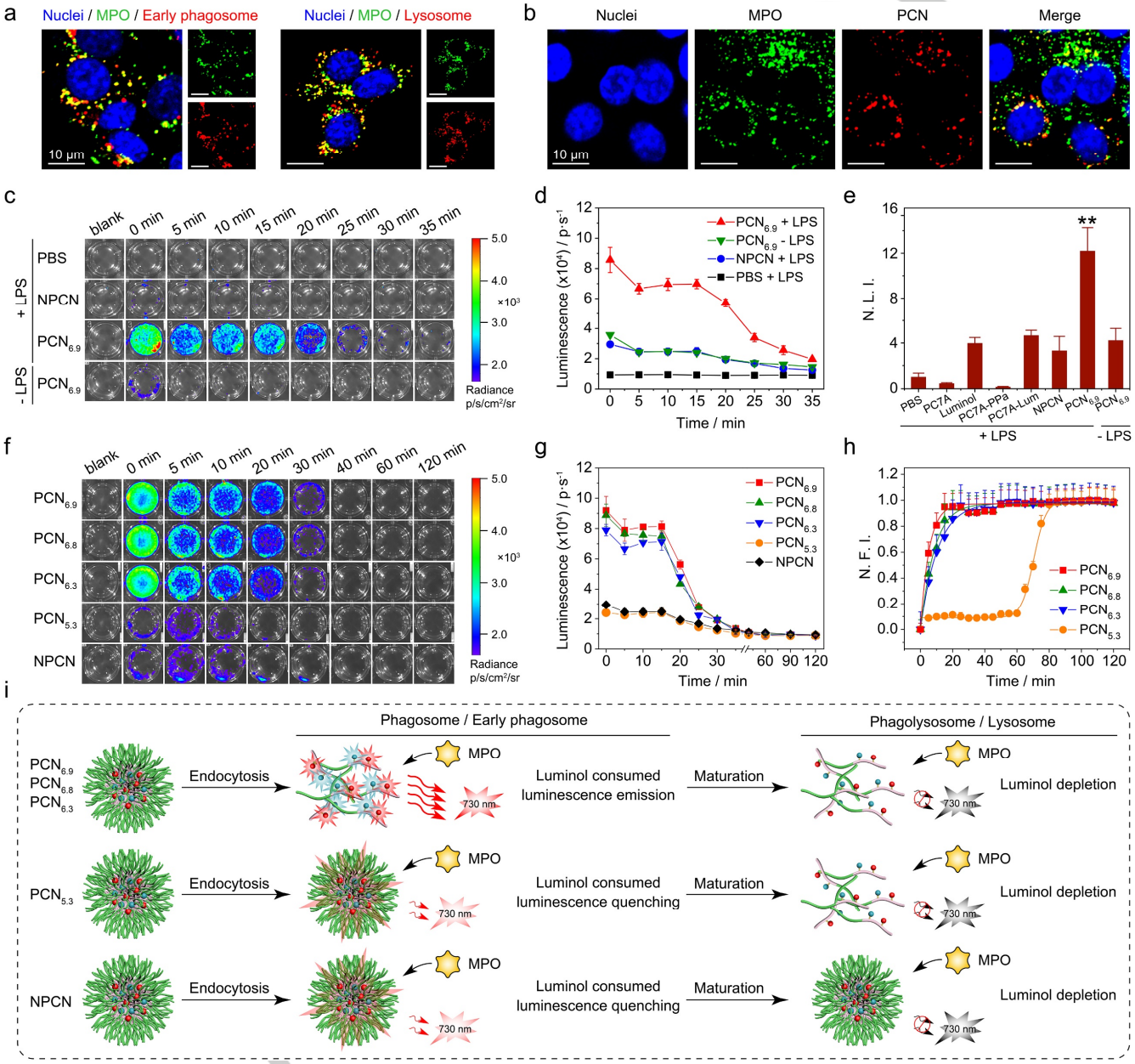

Figure 2. *In vitro* luminescence imaging of inflammatory macrophages. a, b) subcellular distribution of MPO (a) and PCN (b) in LPS-stimulated Raw 264.7 macrophages. Red color represents the early phagosome, lysosome or PCN signals, green color represents the distribution of MPO, yellow color is an indicator for the colocalization of red and green signals. Early phagosome and lysosome were labeled with CellLight® Early Endosomes-RFP (BacMam 2.0) or CellLight® Lysosomes-GFP (BacMam 2.0) reagents, respecively. MPO was labeled with Alexa Fluor 488-labeled antibody. Scale bar = 10 μm. c) Luminescence images and d) time-dependent luminescence intensity curves of Raw 264.7 cells after incubation with PBS, NPCN or $PCN_{6.9}$, with LPS or without LPS stimulation (n = 3). e) Normalized luminescence intensity (N.L.I.) of Raw 264.7 cells at 30 min after incubation with PBS, PC7A, luminol, PC7A-PPa, PC7A-Lum, NPCN, and $PCN_{6.9}$, respectively. N.L.I. was defined as the ratio of determined luminescence intensity over PBS group (n = 3). f) Luminescence images and g) corresponding luminescence intensity of Raw 264.7 cells at predetermined time points after incubation with 250 μg/mL of $PCN_{6.9}$, $PCN_{6.8}$, $PCN_{6.3}$, $PCN_{5.3}$ or NPCN for 15 min under stimulation with 10 μg/mL of LPS (n = 3). h) Real-time fluorescence activation of PCNs. Fluorescence intensity of Raw 264.7 cells was obtained at predetermined time points after incubation with PCNs for 15 min (n = 3). i) Schematic illustration of pH-responsive CRET signal amplification for PCNs and NPCN in specific phagosome maturation stages into macrophages. All data are represented as mean ± s.d., *P<0.05, **P<0.01.

10.1002/anie.202102044

probe, Ce6, which has similar spectral properties to PPa, was also conjugated to PC7A-Lum polymer to show the universality of CRET nanoparticle design. We also found that the synthesized PC7A-Lum-Ce6 nanoparticle showed good luminescence properties (Figure S11).

We next evaluated the pH-dependent amplification of luminescence for other PCNs, including $PCN_{6.8}$, $PCN_{6.3}$, and $PCN_{5.3}$ (Figure S12). All these nanosensors exhibited good pH-dependent luminescence ON/OFF pattern. For quantitative analysis, we plotted the normalized luminescence intensities (N.L.I.) versus pH profiles, where N.L.I. was calculated as the ratio of $(L\text{-}L_{min})/(L_{max}\text{-}L_{min})$ (Figure 1j).[30] The pH_t values were calculated to be 6.75, 6.35, and 5.45 for $PCN_{6.8}$, $PCN_{6.3}$, and $PCN_{5.3}$, respectively, consistent with pK_a values of corresponding polymers. Moreover, R_L and L_{max} for each PCN were also obtained and summarized in Figure 1k and Table S3. $PCN_{6.8}$, $PCN_{6.3}$, and $PCN_{5.3}$ displayed 9.56, 7.80, and 5.18 folds of luminescence amplification capacity, respectively. As a control, pH-nonresponsive NPCN presented the lowest L_{max} and negligible signal enhancement (1.07-fold).

In vitro luminescence imaging of inflammatory macrophages

Macrophages are one of the most important barrier cells in lymph nodes,[31] which have been demonstrated to be widely activated, recruited and proliferated once disease is triggered.[32]

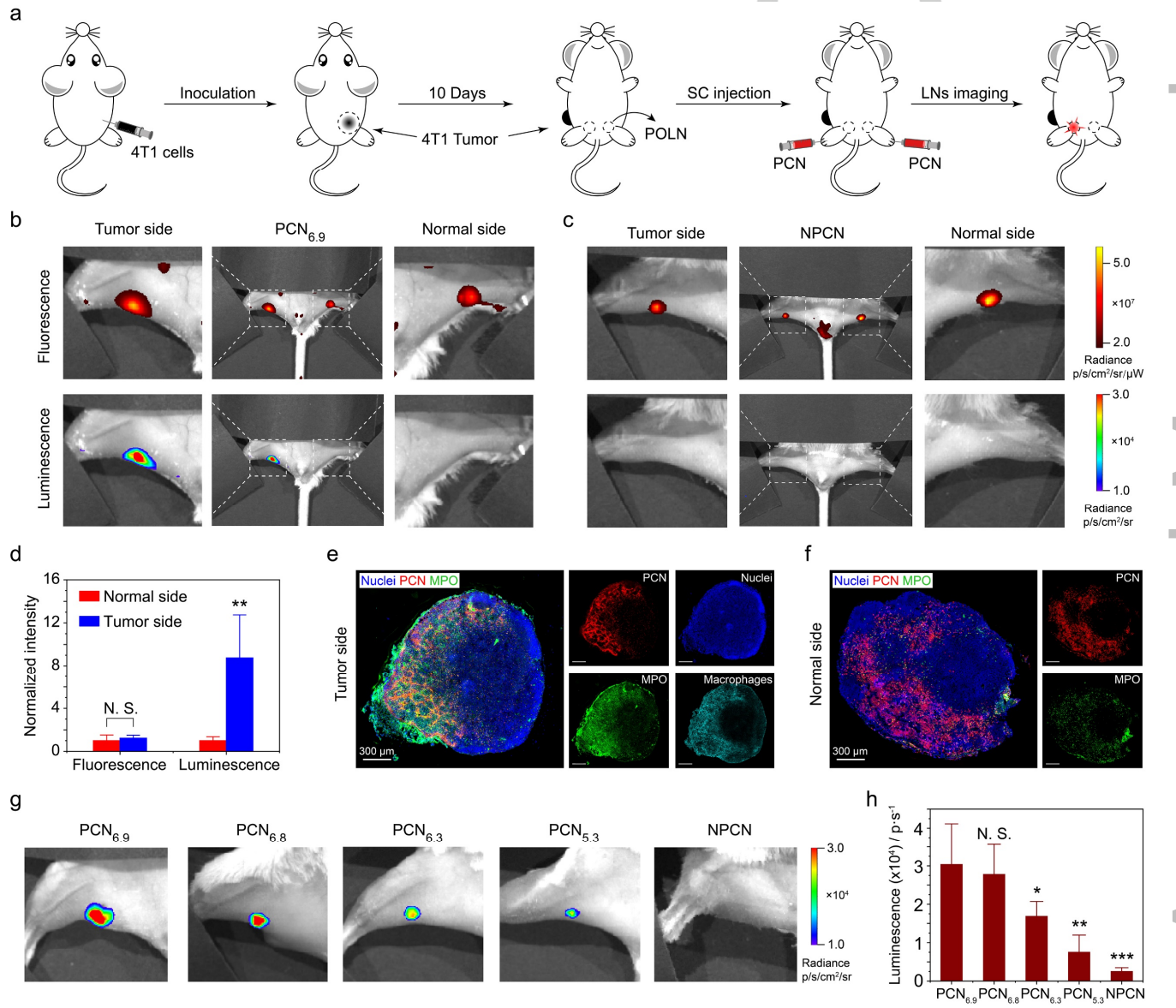

Figure 3. *In vivo* imaging of metastatic tumor-induced inflammatory sentinel lymph nodes. a) Schematic illustration of establishment of 4T1 popliteal lymph node (POLN) metastasis model and luminescence imaging of inflammatory lymph nodes. b, c) Fluorescence imaging (up) and luminescence imaging (down) of POLNs at tumor and normal sides. The mice were subcutaneously injected with $PCN_{6.9}$ (b) or NPCN (c) in the hind paws. d) Quantitative analysis of fluorescence and luminescence intensity in POLNs treated with $PCN_{6.9}$. Signals on the tumor sides were normalized to normal sides (n = 6). e, f) Full landscape scanning of POLNs on the tumor sides (e) and normal sides (f) dissected from mice treated with TMR-labelled $PCN_{6.9}$ nanoparticles. Blue, green, and red signals represent the nuclei, MPO, and $PCN_{6.9}$ nanoparticles, respectively. The distribution of macrophages was also analyzed in an adjacent section. The merged image does not contain macrophage signal. Scale bar = 300 μm. g) Luminescence imaging of POLNs at tumor sides. The mice were subcutaneously injected with $PCN_{6.8}$, $PCN_{6.3}$, $PCN_{5.3}$, and NPCN in the hind paws. h) Quantitative analysis of luminescence intensity of POLNs at tumor sides after injection with PCNs. Images were acquired with the same intensity and exposure time. All data are represented as mean ± s.d., n.s.: no significance, *P<0.05, **P<0.01, ***P<0.001.

For *in vitro* experiments, we firstly cultured inflammatory macrophages, which overexpress MPO upon activation.[33] Weexplored the subcellular distribution of MPO in LPS-induced inflammatory macrophages.[34] Raw 264.7 macrophages were transfected with fluorescent protein (GFP or RFP)-fused Rab5a and Lamp1 for the fluorescently labeling of early phagosome and lysosome, respectively. Confocal images revealed that MPO was widely distributed in the phagosome and lysosomes of macrophages (Figure 2a).[35] PCNs could be efficiently phagocytosed by activated macrophages, and a good colocalization between PCNs and MPO in these macrophages was also observed (Figure 2b).

We next explored the luminescence profile of PCN in macrophages *in vitro*. As shown in Figure 2c, strong luminescence signal was detected in LPS-stimulated macrophages[36] incubated with $PCN_{6.9}$. In contrast, almost no luminescence signal was observed in a series of control groups, including PBS, PC7A, and PC7A-PPa polymers. For PC7A-Lum group, without the energy transfer to PPa, the short emission wavelength hampered the acquisition of signals due to poor transmission of blue light (Figure S13). In particular, since NPCN could not be disassembled after phagocytosis, no obvious self-luminescence signal could be detected as a result of the consumption of luminol in the ACQ state of PPa. For the macrophages without LPS stimulation, the luminescence signal was also significantly suppressed in the absence of activated MPO. Quantitative results indicated that MPO in activated macrophages caused a significant and time-dependent luminescence signal enhancement with peaking time at approximately 10-15 min after incubation (Figure 2d). In addition, PCN exhibited significantly stronger luminescence signal for about 30 min as compared with other groups, with more than 10 times stronger than that of PBS group at 30 min post-incubation, providing sufficient time window for *in vivo* imaging (Figure 2e).

We also cultured 4T1 cells, a mouse breast cancer cell line without MPO expression, as a negative control (Figure S14). We only detected a baseline-level signal from the beginning to the end after incubating with PCN, and the intensity was almost the same as the non-luminescent PC7A-PPa, although fluorescence images indicated that PCN can be efficiently taken up by 4T1 cells. These results demonstrated that PCN can specifically amplify the pathological MPO signals for the luminescence imaging of inflammatory macrophages rather than tumor cells.

Since PCNs can be efficiently taken up by macrophages, the activation of those nanoparticles during phagosome maturation process would be closely related to the signal amplification.[37] Therefore, we then performed luminescence imaging of PCNs with different pH_t in inflammatory macrophages. As shown in Figure 2f, $PCN_{6.9}$, $PCN_{6.8}$, and $PCN_{6.3}$ emitted a relatively dazzling luminescence for about 30 min. Whereas, $PCN_{5.3}$ only released negligible luminescence signals within 2 h incubation (Figure 2g). To explain the above phenomenon, fluorescence activation of PCNs in macrophages was imaged in real time (Figure S15). As shown in Figure 2h, it took more than 60 min for $PCN_{5.3}$ to entirely activate the fluorescence signal. In comparison, the other three nanosensors only need about 15-20 min for fully activation. These results indicated that once PCNs were phagocytosed into macrophages, MPO in the phagosome will immediately catalyze the luminescence emission of luminol regardless of PCNs disassembly or not. Thus, luminol in $PCN_{5.3}$ was fully consumed before nanoparticle dissociation, resulting in diminished PPa luminescence signal due to the ACQ effect. Furthermore, an additional experiment was performed to support our understanding (Figure S16). Firstly, the luminol consumption was imaged in real time at dissociation state of PCNs. Results revealed that the luminol can be consumed within 30 min. Then, the luminescence of $PCN_{5.3}$ was carried out in the micelle state at pH 6.5. As predicted, there was no luminescence emitted. After 30 min, the pH of solution was adjusted to 5.0. However, still no luminescence signal was detected. Collectively, an efficient CRET luminescence amplification can be achieved in PCNs with pH_t ranging from 6.3-6.9, which can be dissociated in phagosome (pH ~ 6.2) of inflammatory macrophages as shown in the proposed mechanism (Figure 2i).[38] In further experiment, we selected $PCN_{6.9}$ for *in vivo* imaging experiments.

In vivo luminescence imaging of tumor metastatic lymph nodes

Having proved the luminescence imaging potential of $PCN_{6.9}$ for inflammatory macrophages *in vitro*, we next investigated its imaging efficacy for tumor metastatic lymph nodes, which have a mass of MPO-overexpressed macrophages regardless of tumor types.[39] A lymphatic metastasis model was established by subcutaneous inoculation of 4T1 tumor cells into the right flank of mice (Figure 3a).[29b] Efficient drainage of $PCN_{6.9}$ to popliteal lymph nodes (POLN) was verified through intradermal injection of $PCN_{6.9}$ in the hind paws of mice (Figure S17).[40] Tumor-bearing mice were intradermally injected with $PCN_{6.9}$ in the left and right hind paws. Fluorescence images exhibited that $PCN_{6.9}$ can efficiently delineate the areas of the POLN in both sides (Figure 3b). However, quantitative results showed no significant difference between the tumor side and normal side (Figure 3d). We also performed luminescence imaging of these POLNs. Surprisingly, luminescence imaging of POLNs displayed a black and white pattern in both sides (Figure 3b). In tumor side, a significant dazzling luminescence was detected, which was colocalized with the fluorescence signals. In contrast, no luminescence signal was detected in the normal site, even though preferential accumulation and activation of $PCN_{6.9}$ in this area. The luminescence signal for POLN in tumor site was up to 10-fold higher than that of normal site (Figure 3d). Additionally, pH-insensitive NPCN failed to luminescently image SLNs regardless of tumor metastasis or not (Figure 3c). It is noteworthy that $PCN_{6.9}$ was injected into the hind paw of tumor bearing mice at a luminol dose of 12 μg per mouse for luminescence imaging of tumor metastatic lymph nodes, which is a relatively low dose as compared with other luminol-contained system.[13b, 41]

After *in vivo* imaging, both sides of POLNs were collected and frozen sectioned. The landscape images of POLNs in the tumor side indicated a significant increase in MPO expression as compared with normal side (Figure 3e and 3f). Interestingly, PCNs were mainly distributed at the afferent area of the lymph nodes,[42] and exhibited a good co-localization with MPO and macrophages. These results demonstrated that the presence of tumors indeed induced the inflammation of SLNs.

We next parallelly compared the SLNs imaging efficacy for a series of PCNs, including $PCN_{6.9}$, $PCN_{6.8}$, $PCN_{6.3}$, $PCN_{5.3}$, and NPCN (Figure 3g). In accordance with the luminescence imaging of inflammatory macrophages *in vitro* (Figure 2f), the imaging efficacy of these five PCNs for SLNs was also highly correlated with pH_t. The quantitative results showed that the higher the pH_t of PCNs, the stronger the luminescence intensity in SLNs, and

10.1002/anie.202102044

thus resulting in more sensitive detection of metastatic lymph nodes (Figure 3h). These results further demonstrated the importance of prompt disassmbly of PCN in acidic phagosome for the amplification of luminescence signals after phagocytosis by macrophages.

PCNs profiles lymphatic metastasis in tumor progression

Having proved the ability of PCNs to specifically and sensitively image metastatic lymph nodes, we then examine whether the PCNs can report the early lymphatic metastasis during tumor progression (Figure 4). A series of balb/c mice bearing different volumes of 4T1-GFP tumors (50-1000 mm^3) were established for luminescence imaging experiments. The mice were intradermally injected in the right hind paws with $PCN_{6.9}$ at a luminol dose of 12 μg per mouse. Then, the fluorescence and luminescence images were simultaneously captured by IVIS imaging system. The tumor size, fluorescence, and luminescence images of several representative mice were shown in Figure 4a and 4b. Strong luminescence signals from lymph nodes were monitored when the 4T1 tumor volume reached up to 200 mm^3. Furthermore, $PCN_{6.9}$ exhibited excellent correlation between luminescence intensity in SLNs and primary tumor volumes. In contrast, for all the tumor-bearing mice, high fluorescence signals

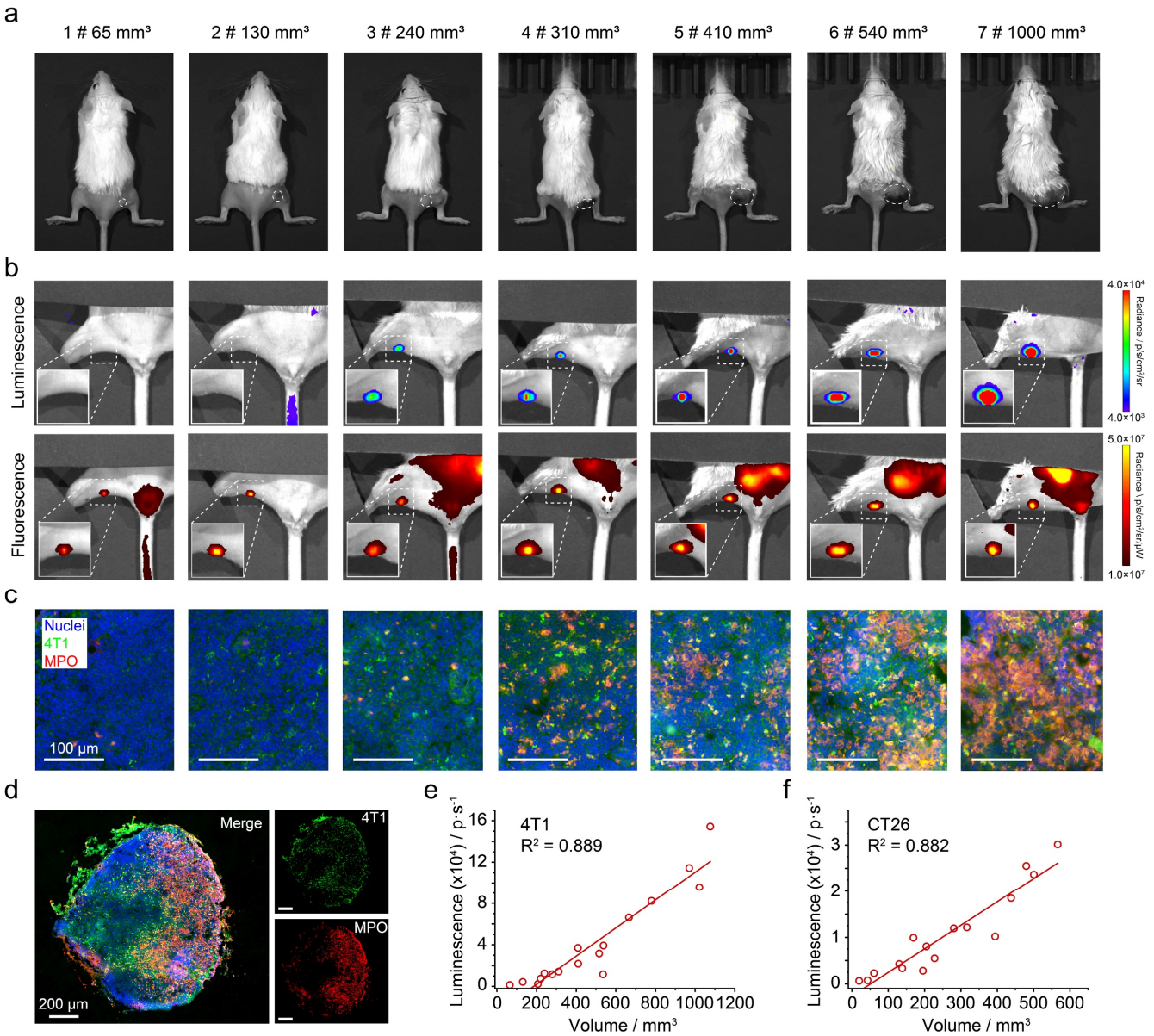

Figure 4. PCN identifies lymphatic metastasis status in tumor progression. a) Appearance images of mice bearing different volumes of 4T1-GFP subcutaneous tumors. The dotted line indicates the area of the tumors. b) Luminescence and fluorescence imaging of the POLNs in Balb/c mice corresponding to a). The mice were intradermally treated with $PCN_{6.9}$ in the hind paws. c) Immunofluorescence staining of POLNs dissected from the mice corresponding to a). Blue, green, and red signals represent the nuclei, metastatic 4T1-GFP tumor cells, and MPO expression, respectively. Scale bar = 100 μm. d) Full landscape scanning of POLNs dissected from mice bearing large 4T1-GFP tumors (~1000 mm^3). Blue, green, and red signals represent the nuclei, 4T1-GFP tumor cells, and MPO expression, respectively. Scale bar = 200 μm. e) and f) Correlation analysis between tumor volume and luminescence intensity of POLNs in $PCN_{6.9}$ treated e) 4T1 tumor bearing mice and f) CT26 tumor bearing mice (n = 16). The tumor size was measured with a digital vernier caliper, and the tumor volume was calculated as Volume (mm^3) = length × $width^2$ × 0.5. Both images were acquired with the same intensity and exposure time.

were detected in the POLNs and other non-tumor areas, suggesting the low specificity of fluorescence imaging for metastatic lymph nodes.

To further explore whether the enhanced luminescence intensity was caused by MPO over-expression in tumor metastatic lymph nodes, we collected and sectioned the corresponding POLNs from mice with different tumor sizes, and performed immunofluorescence analysis. As shown in Figure 4c, the mice with larger tumors presented more tumor cells metastasis into the SLNs, and the higher MPO expression. Landscape images of SLN dissected from mice bearing large 4T1-GFP tumors exhibited a good colocalization of tumor cell infiltration with MPO expression into SLNs (Figure 4d). For the 4T1-GFP tumor reached a volume of 200 mm^3, a small amount of tumor cells was infiltrated into lymph nodes. Accordingly, MPO expression was significantly enhanced, which resulted in the enhanced luminescence signal for early metastasis detection. In another mice model bearing CT26-GFP tumors, the same trend as the 4T1 tumor model was observed (Figure S18). Quantitative results showed a good linear relationship between the tumor volume and the luminescence intensity both in 4T1 (Figure 4e) and CT26 (Figure 4f) tumor-bearing mice models. Collectively, this finding confirmed that PCN can amplify MPO signal in inflammatory lymph nodes for early detection of tumor lymphatic micrometastasis.

Conclusion

In summary, we successfully engineered pH-amplified CRET nanosensors for accurate and sensitive identification of tumor metastasis status in SLNs. The nanoparticles exploit luminol and PPa as CRET donor and acceptor to achieve high intramolecular energy transfer for NIR luminescence emission. The pH-responsive design allows the prompt signal amplification in the acidic phagosome upon phagocytosis by inflammatory macrophages for sensitive *in vivo* imaging. The integrated CRET-signal amplification strategy provided excellent *in vivo* imaging outcome for identification of tumor metastatic lymph nodes. To the best of our knowledge, we report the first pH-responsive CRET nanoparticle imaging strategy and demonstrate that phagosome-targeted CRET nanoparticles significantly amplify the luminescence signals for visualization of metastatic lymph nodes.

Acknowledgements

This work was financially supported by the National Key Research and Development Program of China (2016YFA0201400 and 2017YFA0205600), the National Natural Science Foundation of China (NSFC) Grants (81973260 and 81903554), and Beijing Natural Science Foundation (JQ19025).

Keywords: inflammation, luminescence imaging, tumor metastasis, sentinel lymph nodes, pH responsiveness

[1] G. A. Kwong, G. von Maltzahn, G. Murugappan, O. Abudayyeh, S. Mo, I. A. Papayannopoulos, D. Y. Sverdlov, S. B. Liu, A. D. Warren, Y. Popov, D. Schuppan, S. N. Bhatia, *Nat Biotechnol* **2013**, *31*, 63-70.

[2] D. L. Morton, J. F. Thompson, A. J. Cochran, N. Mozzillo, R. Elashoff, R. Essner, O. E. Nieweg, D. F. Roses, H. J. Hoekstra, C. P. Karakousis, D. S. Reintgen, B. J. Coventry, E. C. Glass, H. J. Wang, M. Group, *N Engl J Med* **2006**, *355*, 1307-1317.

[3] M. Mahesh, M. Madsen, *J Am Coll Radiol* **2017**, *14*, 681-683.

[4] R. Layeeque, J. Kepple, R. S. Henry-Tillman, L. Adkins, R. Kass, M. Colvert, R. Gibson, A. Mancino, S. Korourian, V. S. Klimberg, *Ann Surg* **2004**, *239*, 841-845; discussion 845-848.

[5] aN. Nishio, N. S. van den Berg, S. van Keulen, B. A. Martin, S. Fakurnejad, N. Teraphongphom, S. U. Chirita, N. J. Oberhelman, G. Lu, C. E. Horton, M. J. Kaplan, V. Divi, A. D. Colevas, E. L. Rosenthal, *Nat Commun* **2019**, *10*, 5044; bN. K. Tafreshi, S. A. Enkemann, M. M. Bui, M. C. Lloyd, D. Abrahams, A. S. Huynh, J. Kim, S. R. Grobmyer, W. B. Carter, J. Vagner, R. J. Gillies, D. L. Morse, *Cancer Res* **2011**, *71*, 1050-1059; cX. Yang, Z. Wang, F. Zhang, G. Zhu, J. Song, G. J. Teng, G. Niu, X. Chen, *Theranostics* **2017**, *7*, 153-163.

[6] M. Gerlinger, A. J. Rowan, S. Horswell, M. Math, J. Larkin, D. Endesfelder, E. Gronroos, P. Martinez, N. Matthews, A. Stewart, P. Tarpey, I. Varela, B. Phillimore, S. Begum, N. Q. McDonald, A. Butler, D. Jones, K. Raine, C. Latimer, C. R. Santos, M. Nohadani, A. C. Eklund, B. Spencer-Dene, G. Clark, L. Pickering, G. Stamp, M. Gore, Z. Szallasi, J. Downward, P. A. Futreal, C. Swanton, *N Engl J Med* **2012**, *366*, 883-892.

[7] I. Stoffels, S. Morscher, I. Helfrich, U. Hillen, J. Leyh, N. C. Burton, T. C. Sardella, J. Claussen, T. D. Poeppel, H. S. Bachmann, A. Roesch, K. Griewank, D. Schadendorf, M. Gunzer, J. Klode, *Sci Transl Med* **2015**, *7*, 317ra199.

[8] aC. A. Klein, *Nat Rev Cancer* **2009**, *9*, 302-312; bS. A. Stacker, S. P. Williams, T. Karnezis, R. Shayan, S. B. Fox, M. G. Achen, *Nat Rev Cancer* **2014**, *14*, 159-172; cH. Peinado, H. Zhang, I. R. Matei, B. Costa-Silva, A. Hoshino, G. Rodrigues, B. Psaila, R. N. Kaplan, J. F. Bromberg, Y. Kang, M. J. Bissell, T. R. Cox, A. J. Giaccia, J. T. Erler, S. Hiratsuka, C. M. Ghajar, D. Lyden, *Nat Rev Cancer* **2017**, *17*, 302-317.

[9] C. Zhang, X. Yu, L. Gao, Y. Zhao, J. Lai, D. Lu, R. Bao, B. Jia, L. Zhong, F. Wang, Z. Liu, *Theranostics* **2017**, *7*, 4276-4288.

[10] A. Kleijn, J. W. Chen, J. S. Buhrman, G. R. Wojtkiewicz, Y. Iwamoto, M. L. Lamfers, A. O. Stemmer-Rachamimov, S. D. Rabkin, R. Weissleder, R. L. Martuza, G. Fulci, *Clin Cancer Res* **2011**, *17*, 4484-4493.

[11] S. Gross, S. T. Gammon, B. L. Moss, D. Rauch, J. Harding, J. W. Heinecke, L. Ratner, D. Piwnica-Worms, *Nat Med* **2009**, *15*, 455-461.

[12] G. Ndrepepa, *Clin Chim Acta* **2019**, *493*, 36-51.

[13] aN. Zhang, K. P. Francis, A. Prakash, D. Ansaldi, *Nat Med* **2013**, *19*, 500-505; bX. Xu, H. An, D. Zhang, H. Tao, Y. Dou, X. Li, J. Huang, J. Zhang, *Sci Adv* **2019**, *5*, eaat2953; cA. J. Shuhendler, K. Pu, L. Cui, J. P. Uetrecht, J. Rao, *Nat Biotechnol* **2014**, *32*, 373-380; dX. Zhen, C. Zhang, C. Xie, Q. Miao, K. L. Lim, K. Pu, *ACS Nano* **2016**, *10*, 6400-6409.

[14] B. Chen, W. Dai, B. He, H. Zhang, X. Wang, Y. Wang, Q. Zhang, *Theranostics* **2017**, *7*, 538-558.

[15] W. Hou, J. W. H. Lou, J. Bu, E. Chang, L. Ding, M. Valic, H. H. Jeon, D. M. Charron, C. Coolens, D. Cui, J. Chen, G. Zheng, *Angew Chem Int Ed Engl* **2019**, *58*, 14974-14978.

[16] Y. Wang, K. Zhou, G. Huang, C. Hensley, X. Huang, X. Ma, T. Zhao, B. D. Sumer, R. J. DeBerardinis, J. Gao, *Nat Mater* **2014**, *13*, 204-212.

[17] Z. T. Bennett., Q. Feng., J. A. Bishop., G. Huang., B. D. Sumer., J. Gao, *Theranostics* **2020**, *10*, 3340-3350.

[18] L. Xiong, A. J. Shuhendler, J. Rao, *Nat Commun* **2012**, *3*, 1193.

[19] J. P. Qi, X. W. Hu, X. C. Dong, Y. Lu, H. P. Lu, W. L. Zhao, W. Wu, *Adv Drug Deliver Rev* **2019**, *143*, 206-225.

[20] Y. Li, Y. Wang, G. Huang, J. Gao, *Chem Rev* **2018**, *118*, 5359-5391.

[21] aK. Zhou, Y. Wang, X. Huang, K. Luby-Phelps, B. D. Sumer, J. Gao, *Angew Chem Int Ed Engl* **2011**, *50*, 6109-6114; bX. Ma, Y. Wang, T. Zhao, Y. Li, L. C. Su, Z. Wang, G. Huang, B. D. Sumer, J. Gao, *J Am Chem Soc* **2014**, *136*, 11085-11092.

[22] B. Panganiban, B. Qiao, T. Jiang, C. DelRe, M. M. Obadia, T. D. Nguyen, A. A. A. Smith, A. Hall, I. Sit, M. G. Crosby, P. B. Dennis, E. Drockenmuller, M. Olvera de la Cruz, T. Xu, *Science* **2018**, *359*, 1239-1243.

[23] H. C. Kang, Y. H. Bae, *Adv Funct Mater* **2007**, *17*, 1263-1272.

[24] R. J. Goiffon, S. C. Martinez, D. Piwnica-Worms, *Nat Commun* **2015**, *6*, 6271.

[25] H. Yuan, H. Chong, B. Wang, C. Zhu, L. Liu, Q. Yang, F. Lv, S. Wang, *J Am Chem Soc* **2012**, *134*, 13184-13187.

[26] N. Boute, R. Jockers, T. Issad, *Trends Pharmacol Sci* **2002**, *23*, 351-354.
[27] N. Keller, M. Calik, D. Sharapa, H. R. Soni, P. M. Zehetmaier, S. Rager, F. Auras, A. C. Jakowetz, A. Gorling, T. Clark, T. Bein, *J Am Chem Soc* **2018**, *140*, 16544-16552.
[28] M. K. So, A. M. Loening, S. S. Gambhir, J. Rao, *Nat Protoc* **2006**, *1*, 1160-1164.
[29] aG. Borghei, E. A. Hall, *Analyst* **2014**, *139*, 4185-4192; bR. Tian, H. Ma, S. Zhu, J. Lau, R. Ma, Y. Liu, L. Lin, S. Chandra, S. Wang, X. Zhu, H. Deng, G. Niu, M. Zhang, A. L. Antaris, K. S. Hettie, B. Yang, Y. Liang, X. Chen, *Adv Mater* **2020**, *32*, e1907365.
[30] K. Zhou, H. Liu, S. Zhang, X. Huang, Y. Wang, G. Huang, B. D. Sumer, J. Gao, *J Am Chem Soc* **2012**, *134*, 7803-7811.
[31] A. Schudel, D. M. Francis, S. N. Thomas, *Nat Rev Mater* **2019**, *4*, 415-428.
[32] T. A. Wynn, A. Chawla, J. W. Pollard, *Nature* **2013**, *496*, 445-455.
[33] S. Thekkan, M. S. Jani, C. Cui, K. Dan, G. Zhou, L. Becker, Y. Krishnan, *Nat Chem Biol* **2019**, *15*, 1165-1172.
[34] I. Kinjyo, T. Hanada, K. Inagaki-Ohara, H. Mori, D. Aki, M. Ohishi, H. Yoshida, M. Kubo, A. Yoshimura, *Immunity* **2002**, *17*, 583-591.
[35] aN. W. M. de Jong, K. X. Ramyar, F. E. Guerra, R. Nijland, C. Fevre, J. M. Voyich, A. J. McCarthy, B. L. Garcia, K. P. M. van Kessel, J. A. G. van Strijp, B. V. Geisbrecht, P. A. Haas, *Proc Natl Acad Sci U S A* **2017**, *114*, 9439-9444; bS. J. Klebanoff, *J Leukoc Biol* **2005**, *77*, 598-625.
[36] Y. Zheng, R. He, P. Wang, Y. Shi, L. Zhao, J. Liang, *Biomater Sci* **2019**, *7*, 2037-2049.
[37] Y. Wang, C. Wang, Y. Li, G. Huang, T. Zhao, X. Ma, Z. Wang, B. D. Sumer, M. A. White, J. Gao, *Adv Mater* **2017**, *29*, 1603794.
[38] D. G. Russell, B. C. Vanderven, S. Glennie, H. Mwandumba, R. S. Heyderman, *Nat Rev Immunol* **2009**, *9*, 594-600.
[39] J. Condeelis, J. W. Pollard, *Cell* **2006**, *124*, 263-266.
[40] E. R. Pereira, D. Kedrin, G. Seano, O. Gautier, E. F. J. Meijer, D. Jones, S. M. Chin, S. Kitahara, E. M. Bouta, J. Chang, E. Beech, H. S. Jeong, M. C. Carroll, A. G. Taghian, T. P. Padera, *Science* **2018**, *359*, 1403-1407.
[41] aH. Tao, J. Guo, Y. Ma, Y. Zhao, T. Jin, L. Gu, Y. Dou, J. Liu, H. Hu, X. Xiong, J. Zhang, *ACS Nano* **2020**, *14*, 11083-11099; bR. Liu, J. Tang, Y. Xu, Z. Dai, *ACS Nano* **2019**, *13*, 5124-5132.
[42] L. A. Johnson, D. G. Jackson, *Ann N Y Acad Sci* **2008**, *1131*, 119-133.

10.1002/anie.202102044

WILEY-VCH

RESEARCH ARTICLE

Entry for the Table of Contents

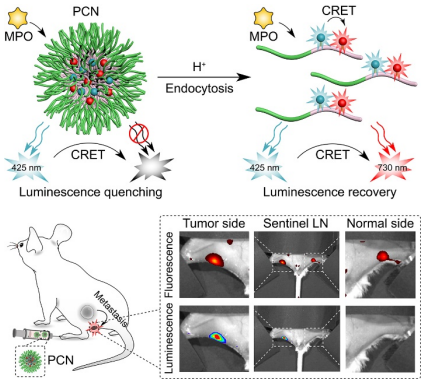

A series of pH-amplified self-illuminating nanoprobes dually respond to acidity and myeloperoxidase of phagosome in inflammatory macrophages were synthesized. The nanoparticles exhibit excellent imaging capability for identification of metastatic sentinel lymph nodes in diverse animal tumor models.